Quantum and Quasi-classical Dynamics of the $C(^3P) + O_2(^3\Sigma_g^-) \rightarrow CO(^1\Sigma^+) + O(^1D)$ Reaction on Its Electronic Ground State

Sugata Goswami, Juan Carlos San Vicente Veliz, Meenu Upadhyay,[†] Raymond J. Bemish,[‡] and Markus Meuwly[*,†,¶]

[†]*Department of Chemistry, University of Basel, Klingelbergstrasse 80, CH-4056 Basel, Switzerland*

[‡]*Air Force Research Laboratory, Space Vehicles Directorate, Kirtland AFB, New Mexico 87117, USA*

[¶]*Department of Chemistry, Brown University, RI, USA*

E-mail: m.meuwly@unibas.ch

June 23, 2022

Abstract

The dynamics of the $C(^3P) + O_2(^3\Sigma_g^-) \rightarrow CO(^1\Sigma^+) + O(^1D)$ reaction on its electronic ground state is investigated by using time-dependent wave packet propagation (TDWP) and quasi-classical trajectory (QCT) simulations. For the moderate collision energies considered ($E_c = 0.001$ to 0.4 eV, corresponding to a range from 10 K to 4600 K) the total reaction probabilities from the two different treatments of the nuclear dynamics agree very favourably. The undulations present in $P(E)$ from the quantum mechanical treatment can be related to stabilization of the intermediate CO_2 complex

with lifetimes of on the 0.05 ps time scale. This is also confirmed from direct analysis of the QCT trajectories. Product diatom vibrational and rotational level resolved state-to-state reaction probabilities from TDWP and QCT simulations also agree well except for the highest product vibrational states ($v' \geq 15$) and for the lowest product rotational states ($j' \leq 10$). Opening of the product vibrational level CO($v' = 17$) requires ~ 0.2 eV from QCT and TDWP simulations with $O_2(j = 0)$ and decreases to 0.04 eV if all initial rotational states are included in the QCT analysis, compared with $E_c > 0.04$ eV obtained from experiments. It is thus concluded that QCT simulations are suitable for investigating and realistically describe the $C(^3P) + O_2(^3\Sigma_g^-) \rightarrow CO(^1\Sigma^+) + O(^1D)$ reaction down to low collision energies when compared with results from a quantum mechanical treatment using TDWPs.

1 Introduction

Reactions involving carbon and oxygen atoms play a vital role in the atmosphere, in combustion, and in hypersonic flow.[1] Among all, the $C(^3P) + O_2(^3\Sigma_g^-) \longleftrightarrow CO(^1\Sigma^+) + O(^1D)/O(^3P)$ reaction involving the CO_2 intermediate and several electronic states is particularly important and has, therefore, been investigated both, experimentally and through computations.[2–21] The electronic ground and excited state potential energy surfaces (PESs) were studied computationally in detail at different levels of theory[12,21–27] and various dynamics simulations were also carried out for this system.[13,15,21,28,29]

One of the latest investigations for the entire $C(^3P) + O_2(^3\Sigma_g^-) \longleftrightarrow CO_2 \longleftrightarrow CO(^1\Sigma^+) + O(^1D)/O(^3P)$ reaction was carried out using quasi-classical trajectory (QCT) simulations with kernel-represented PESs based on extensive multi reference configuration interaction (MRCI) calculations.[21] The focus was more on the high-temperature regime of the reaction also because experimental and computational data from shock tube experiments for the $C + O_2 \rightarrow CO + O$ reaction between 1500-4200 K was available.[9,13] The latest QCT simula-

tions reported the forward and backward thermal rates for the lowest five electronic states together with vibrational relaxation times.[21] However, the state-to-state dynamics was not considered and the question remains whether a classical framework is suitable when compared with results from a quantum mechanical treatment of the nuclear dynamics.

One recurrent theme for atom + diatom reactions concerns the range of applicability of quasi-classical-based dynamics approaches for computing thermal rates and final state distributions. Cross sections and thermal rates are averaged over initial and/or final ro-vibrational resolved state-to-state information. Thus, although more or less heavily averaged quantities may favourably agree between different approaches, it is possible that such agreement arises from the averaging process. Hence, it is also relevant to compare properties at the state-to-state level. All such quantities are essential as input to more coarse-grained investigations of reaction networks as they appear in hypersonics, combustion, atmospheric and astrophysical chemistry.[30] Because QCT simulations are computationally more efficient, they are often used instead of and also along with more time-consuming quantum nuclear dynamics simulations.[31–35]

Quantum mechanical and QCT approaches were used to evaluate reaction probabilities and rates for the C+OH reaction and were found to be in fairly good agreement.[36–38] For the S+OH reaction quantum mechanical and QCT simulations produced excellent agreement for cross sections but only fair agreement for the total reaction probabilities and thermal rates.[32,39] Comprehensive QCT and QM dynamics investigations for the Br + H_2 and O + HCl reactions reported favourable agreement between QM and QCT results for properties such as reaction probabilities, integral and differential cross sections.[40,41] Similar to the S+OH reaction, for N + H_2 results from QM and QCT simulations agree favourably for cross sections but not so well for reaction probabilities.[42]

For the S+OH reaction it has been specifically reported that for reactive collisions a more general relationship between the mechanistic details of the dynamics and the ensuing rates can be difficult to obtain.[32] Nonetheless, it is generally believed that the dynamical features of an exoergic and barrierless reaction primarily depend on the masses of the participating atoms, the exoergicity and the topographical details of the underlying PES.[32,43,44] To better understand the origins of the observed dynamics systematic investigations have been carried out for different systems.[38,43–47] As an example, for the C + OH reactive collisions[38,43,44] it was found that reagent vibrational excitation decreased reactivity on the first electronically excited PES and enhances reactivity on the second excited state. The excess vibrational energy is transferred into product translational energy for the first excited PES whereas for the second excited state it is transferred into product vibration and rotation. These dynamical effects on the final states are caused by the topology of the underlying PESs which have no barrier to products for the first electronically excited state but involve a late barrier for the second excited state.

The reaction $C(^3P) + O_2(^3\Sigma_g^-) \rightarrow CO(^1\Sigma^+) + O(^1D)/O(^3P)$ using its five lowest lying states ($^1A'$, $^3A'$, $^3A''$, $^1A''$ and $(2)^1A'$) is a particularly suitable system for such an investigation due to the availability of high-quality, full-dimensional PESs which were recently validated vis-a-vis experiment.[21] The exoergicity of the three singlet and two triplet states are ~ 3.8 eV and ~ 5.9 eV, respectively.[21] Therefore, the difference in the dynamical attributes on the singlet and triplet states is expected to arise solely from the topographical details of the underlying surfaces.[32]

Quantum mechanics-based dynamics approaches can become computationally expensive for barrierless exoergic reactions with deep wells.[32,38,43,44,48,49] Thus, QCT approaches are an attractive alternative, at least at the qualitative level. In the present work the initial state-selected and state-to-state reaction probabilities for the $C(^3P) + O_2(^3\Sigma_g^-) \rightarrow CO(^1\Sigma^+)+$

O(^{1}D) reaction on the electronic ground (^{1}A$'$) state are determined for low to moderate collision energies ($E_c \leq 0.4$ eV) by TDWP and QCT approaches. Total reaction probabilities and final state distributions are determined for a range of collision energies and allow to compare the two dynamics methods in terms of their findings and with experiment. The work is organized as follows. First the methods used are described. Then, the convergence of the TDWP simulations is assessed, followed by results for the total reaction probabilities and the product vibrational resolved reaction probabilities from TDWP and QCT simulations. Next, product vibrational and rotational state distributions are determined and compared. Finally, the computational results are discussed in the context of experiments and in a broader sense.

2 Methods

2.1 Time Dependent Wavepacket Calculations

State-to-state quantum dynamics was investigated using the modified DIFFREALWAVE code which is based on propagating real wave packets (RWP).[50,51] Here only a summary of the method employed is given as the theory has been described extensively elsewhere.[44,50–53] The RWP approach is advantageous from a computational perspective as the formalism requires only the real part of the wave packet (WP) to be propagated for obtaining the state-to-state S-matrix elements. An initial WP, $q_A(R_A, r_A, \gamma_A, t = 0)$ is prepared in the asymptotic reactant channel with the geometry described in a Jacobi coordinate system (R_A: distance of atom A from the center-of-mass of BC, r_A: BC internuclear distance and γ_A: approach angle of A to the center-of-mass of BC), see Figure 1. The real part of such a WP in this coordinate system takes the form[44,52,53]

$$q_A(R_A, r_A, \gamma_A, t = 0) = \frac{\sin[\alpha(R_A - R_0)]}{R_A - R_0} \cos[k_0(R_A - R_0)] e^{-\beta_s (R_A - R_0)^2} \phi_{vj}^{BC}(r_A) P_j^{\Omega}(\cos\gamma_A) \quad (1)$$

The parameters α and β_s define the width and the smoothness of the WP, respectively,[54] k_0 is the initial momentum of the WP centered at R_0, $\phi_{vj}^{\rm BC}$ and $P_j^{\Omega}(\cos\gamma_a)$ represent the ro-vibrational eigenfunction of BC and the associated Legendre polynomials, respectively, and v and j are the initial vibrational and rotational levels of the reactant diatom.

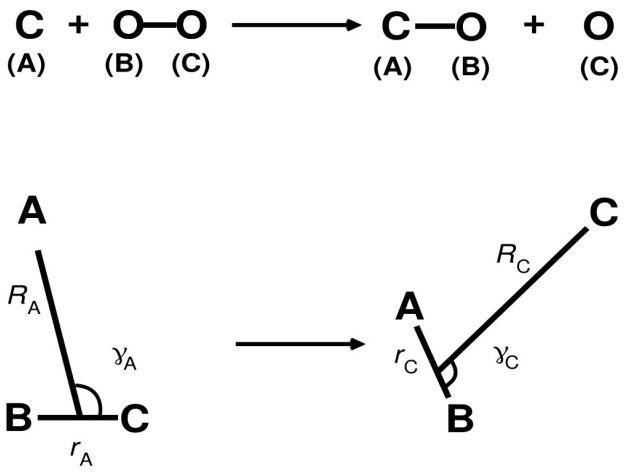

Figure 1: Reactant (left) and product (right) collision geometries in body-fixed Jacobi coordinates for the present TDWP simulations.

The initial WP (Eq. (1)) is subsequently transformed to product state Jacobi coordinates ($R_{\rm C}$, $r_{\rm C}$, $\gamma_{\rm C}$) with C as atom and AB as diatom, see right-bottom part of Figure 1, according to[52]

$$q_{\rm C}^{J\Omega'}(R_{\rm C}, r_{\rm C}, \gamma_{\rm C}, t=0) = N\sqrt{w_{\rm C}}q_{\rm A}(R_{\rm A}, r_{\rm A}, \gamma_{\rm A}, t=0)\frac{R_{\rm C}r_{\rm C}}{R_{\rm A}r_{\rm A}}d^J_{\Omega\Omega'}(\beta). \qquad (2)$$

Here N, $d^J_{\Omega\Omega'}(\beta)$, β and Ω' are normalization, the reduced Wigner matrix, the angle between the two vectors, $\mathbf{R}_{\rm C}$ and $\mathbf{R}_{\rm A}$, and the projection of J on the body-fixed Z-axis of the product Jacobi coordinates, respectively.

The action of the nuclear Hamiltonian $\hat{H}_{\rm nuc}$, formulated in product Jacobi coordinates, $\hat{H}_{\rm nuc}$,

on the WP is[52,55]

$$
\begin{aligned}
\hat{H}_{\rm nuc} q_{\rm C}^{J\Omega'}(t) &= \left[-\frac{1}{2\mu_R^{AB,C}} \frac{\partial^2}{\partial R_{\rm C}^2} - \frac{1}{2\mu_r^{AB}} \frac{\partial^2}{\partial r_{\rm C}^2} \right] q_{\rm C}^{J\Omega'}(t) \\
&- \left(\frac{1}{2\mu_R^{AB,C} R_{\rm C}^2} + \frac{1}{2\mu_r^{AB} r_{\rm C}^2} \right) \left[\frac{1}{\sin\gamma_{\rm C}} \frac{\partial}{\partial \gamma_{\rm C}} \sin\gamma_{\rm C} \frac{\partial}{\partial \gamma_{\rm C}} - \frac{\Omega'^2}{\sin^2\gamma_{\rm C}} \right] q_{\rm C}^{J\Omega'}(t) \\
&+ \hat{V}(R_{\rm C}, r_{\rm C}, \gamma_{\rm C}) q_{\rm C}^{J\Omega'}(t) \\
&+ \left(\frac{1}{2\mu_R^{AB,C} R_{\rm C}^2} \right) (J(J+1) - 2\Omega'^2) q_{\rm C}^{J\Omega'}(t) \\
&- \frac{C_{J\Omega'}^{+}}{2\mu_R^{AB,C} R_{\rm C}^2} \left[\frac{\partial}{\partial \gamma_{\rm C}} - \Omega' \cot\gamma_{\rm C} \right] q_{\rm C}^{J(\Omega'+1)}(t) \\
&- \frac{C_{J\Omega'}^{-}}{2\mu_R^{AB,C} R_{\rm C}^2} \left[-\frac{\partial}{\partial \gamma_{\rm C}} - \Omega' \cot\gamma_{\rm C} \right] q_{\rm C}^{J(\Omega'-1)}(t). \qquad (3)
\end{aligned}
$$

Here and in what follows, the coordinate dependence of the WPs, $q_{\rm C}^{J\Omega'}(t)$, $q_{\rm C}^{J(\Omega'+1)}(t)$ and $q_{\rm C}^{J(\Omega'-1)}(t)$ is omitted for clarity. The terms $\mu_R^{AB,C}(=\frac{m_{\rm C}(m_{\rm A}+m_{\rm B})}{(m_{\rm A}+m_{\rm B}+m_{\rm C})})$ and $\mu_r^{AB}(=\frac{m_{\rm A}m_{\rm B}}{(m_{\rm A}+m_{\rm B})})$ represent the three body and product diatom reduced masses, respectively. The action of the radial kinetic energy part of the Hamiltonian is carried out using fast Fourier transformation techniques.[56] For the action of the angular kinetic energy part a discrete variable representation based on Gauss-Legendre quadrature is used.[57–59] The effect of the potential energy operator, $\hat{V}(R_{\rm C}, r_{\rm C}, \gamma_{\rm C})$, on the WP is multiplicative on the coordinate grid and the last two terms of Eq. (3) denote the Coriolis coupling and lead to mixing of the WP, $q_{\rm C}^{J\Omega'}$ with other WPs, $q_{\rm C}^{J(\Omega'+1)}$ and $q_{\rm C}^{J(\Omega'-1)}$ as shown in the Eq. (3).

The propagated WP at the first time step, τ_1, is evaluated according to

$$
q_{\rm C}^{J\Omega'}(\tau_1) = \hat{H}_{\rm nuc,s} q_{\rm C}^{J\Omega'}(0) - \sqrt{1 - \hat{H}_{\rm nuc,s}^2}\, p_{\rm C}^{J\Omega'}(0), \qquad (4)
$$

where $p_{\rm C}^{J\Omega'}$ denotes the imaginary part of the initial WP (see Eq. (1) and (2)). For the

subsequent time propagation a three term recursion is used

$$q_{\mathrm{C}}^{J\Omega'}(t+\tau) = -q_{\mathrm{C}}^{J\Omega'}(t-\tau) + 2\hat{H}_{nuc,s}q_{\mathrm{C}}^{J\Omega'}(t), \tag{5}$$

where τ is the discrete time step. In Eq. (4) and (5), $\hat{H}_{nuc,s}$ represents the scaled and shifted Hamiltonian whose minimum and maximum eigenvalues lie between -1 and $+1$.[51]

As is customary for TDWP simulations, spurious reflections of the WP components from the finite sized grid edges at longer propagation time need to be damped. This is done by multiplying the wavepacket with a double exponential damping function[52] $a(y)$ along coordinates $y = R_c, r_c$

$$a(y) = \exp[-c_{abs}\exp(-2(y_{max} - y_{abs})/(y - y_{abs}))] \tag{6}$$

according to $q_{\mathrm{C}}^{J\Omega'}(t)\cdot a(R_{\mathrm{C}})\cdot a(r_{\mathrm{C}})$, where c_{abs} and y_{abs} represent the strength and the starting point of the absorption, respectively. The absorption is applicable for $y > y_{abs}$ and the value of the function is equal to 1 elsewhere.

The propagated WP is projected on ro-vibrational levels of the product diatom at the product asymptote ($R = R_\infty$) to obtain the time-dependent coefficients[52]

$$C^J_{v,j,\Omega\rightarrow v',j',\Omega'}(t) = \int \phi^{*AB}_{v',j'}(r_{\mathrm{C}},\gamma_{\mathrm{C}})q_{\mathrm{C}}^{J\Omega'}(R_{\mathrm{C}} = R_\infty, r_{\mathrm{C}},\gamma_{\mathrm{C}},t)dr_{\mathrm{C}}\sin(\gamma_{\mathrm{C}})d\gamma_{\mathrm{C}}. \tag{7}$$

The term, $\phi^{AB}_{v',j'}$ in Eq. (7) represents the (v',j') state of the product diatom AB. The time-dependent coefficients $C^J_{v,j,\Omega\rightarrow v',j',\Omega'}(t)$ are Fourier transformed to obtain energy dependent coefficients, $A^J_{v,j,\Omega\rightarrow v',j',\Omega'}(E)$ in the body fixed frame and then are transformed to the space fixed frame from which the scattering matrix (S-matrix) elements, $S^J_{v,j,l\rightarrow v',j'l'}(E)$ are obtained. These S-matrix elements are finally transferred back to the body-fixed frame to

yield $S^J_{v,j,\Omega\rightarrow v',j'\Omega'}(E)$ from which energy dependent state-to-state reaction probabilities are obtained according to

$$P^J_{v,j,\Omega\rightarrow v',j',\Omega'}(E) = |S^J_{v,j,\Omega\rightarrow v',j',\Omega'}(E)|^2 \tag{8}$$

Product internal level resolved probabilities are calculated by summing up the probabilities of Eq. 8 over relevant quantum numbers. Summation over all three quantum numbers, (Ω', j', v') yields the energy resolved total reaction probabilities. For further details, see Ref. 52.

2.2 Quasi Classical Trajectory Simulations

The QCT simulations in the present investigation were carried following earlier work[21] and based on established procedures.[60–63] Therefore, only specific technical aspects are briefly summarized here.

Hamilton's equations of motion were solved using a fourth order Runge-Kutta method. The initial conditions for initiating the trajectories were sampled by using standard Monte Carlo methods[63] and the ro-vibrational levels of reactant and product diatoms are calculated using semiclassical quantization. The simulations are run at several collision energies with a time step of $\Delta t = 0.05$ fs which guarantees the conservation of total energy and angular momentum. At each collision energy, 5×10^5 trajectories are run for converged results, except at the two lowest energies, 0.0055 and 0.001022 eV for which 10^6 trajectories are run for convergence of the total reaction probability for $O_2(v = 0, j = 0)$. It is found that the difference between the total reaction probabilities at these two energies obtained from 5×10^5 and 10^6 trajectories appears at the fourth decimal place and therefore all remaining calculations are carried out with 5×10^5 trajectory simulations. As the associated quantum numbers are real-valued, their necessary assignment to integer values was made either by using Gaussian binning

(GB)[61,64,65] which centers Gaussian weights around the integer values and has a full width at half maximum of 0.1 or from Histogram binning (HB) which rounds to the nearest integer.

The reaction probability at collision energy E_{col} is obtained as

$$P_{\mathrm{r}}(E_{\mathrm{col}}) = \frac{N_r(E_{\mathrm{col}})}{N_{\mathrm{tot}}(E_{\mathrm{col}})}, \tag{9}$$

where $N_{\mathrm{r}}(E_{\mathrm{col}})$ is the number of reactive trajectories and $N_{\mathrm{tot}}(E_{\mathrm{col}})$ is the total number of trajectories at a give E_{col}.

3 Results and Discussion

3.1 Convergence of the TDWP approach

The TDWP approach is a grid-based method and the results depend on the parameters characterizing the wavepacket and the underlying grids. In a first step, convergence of the total reaction probability was sought for each parameter. For a particular parameter considered (see Table 1) its value was changed until the total reaction probability remained unchanged. The convergence runs were initialized from arbitrary guesses for the parameters and the wave packet propagation was carried out for fewer time steps (25000 in the present case) than for the final production runs. If convergence was not achieved, the WP was propagated for longer times.

Convergence runs for all parameters were carried out for $J = 0$ and for reactant $O_2(v = 0, j = 0)$. The converged parameters are summarized in Table 1 and demonstrate that extensive grids along the three product Jacobi coordinates are required resulting in computationally

Table 1: Details of the numerical parameters related to the coordinate grid, properties of initial wave packet and the damping/ absorption function used in present TDWP investigation of the C + O_2 ($v = 0 - 2$, $j = 0$) $\rightarrow$ CO + O reaction on its electronic ground ($^1A'$) state.

Parameter	Value	Description
$N_R/N_r/N_\gamma$	499/419/240	Number of grid points along the three product Jacobi coordinates, R_C, r_C and γ_C.
R_{min}/R_{max} (a_0)	2.2/22.0	Extension of the grid along R_C
r_{min}/r_{max} (a_0)	1.5/17.9902	Extension of the grid along r_C
R_∞ (a_0)	12.5	Location of the dividing surface in the product channel
R_{abs}/r_{abs} (a_0)	14.0/14.75	Starting point of the absorption function along R_C and r_C
C_{abs}/c_{abs}	30.0/30.0	Strength of the absorption along R_C and r_C
R_0 (a_0)	13.2	Center of the initial wave packet in reactant Jacobi coordinate
E_{trans} (eV)	0.115	Initial translational energy in eV
α	12.0	Width of the initial wave packet
β_s	0.5	Smoothing of the initial wave packet

expensive calculations. The requirement for such large grids is the result of the heavy masses of the interacting atoms and the presence of the deep potential well.[21] The large number of grid points required along the angular Jacobi coordinate reflects the pronounced angular anisotropy of the underlying PES.

Two-dimensional (2-D) contours of the underlying PES are shown in Figure 2. The top row reports the PES in reactant Jacobi coordinates for $R_{OO} = r_A = 3.40$ a_0, i.e. a stretched geometry of the reactant diatom before C-insertion occurs to form O-C-O (minimum at 90°). Because after formation of the triatom the system only spends little time in this state (typically < 0.5 ps, see Discussion section) to move towards the product, it is also of interest to provide a representation of the reactant PES in terms of product Jacobi coordinates (R_C, γ_C) which is shown in the top right panel in Figure 2. Comparison of the two representations clarifies that spatial symmetry is lost for the product state coordinates and the anisotropy

of the PES differs considerably. Similarly, the bottom row reports the PES in product state coordinates for $R_{\mathrm{CO}} = r_{\mathrm{C}} = 3.0$ a$_0$, i.e. for the system on its way to form products (left panel) and the same PES represented in reactant state coordinates $(R_{\mathrm{A}}, \gamma_{\mathrm{A}})$ in the right hand lower panel of Figure 2. In addition, representative structures for CO_2 are reported and their location on the PES are indicated by arrows. Two geometries (see black and purple crosses in the top row panels) are chosen to show their positions in the reactant and equivalent product Jacobi coordinates.

Because converging the wavepacket with $O_2(v = 0, j = 0)$ was laborious, no reoptimization was carried out for $O_2(v = 1, j = 0)$ and $O_2(v = 2, j = 0)$. However, the number of product vibrational levels was suitably increased to $v' = 19$ and $v' = 20$ with the reactant in its two vibrationally excited states. The WP was propagated for up to 70000 time steps (corresponding to ~ 1.4 ps) in order to obtain converged reaction probabilities for $J = 0$ and the potential and/or centrifugal cut-off was $0.57 E_{\mathrm{h}}$.

3.2 Total Reaction Probabilities

Initial state-selected and energy resolved total reaction probabilities of the $C(^3P) + O_2(^3\Sigma_g^-$, $v = 0 - 2$, $j = 0) \rightarrow CO(^1\Sigma^+, \sum v', \sum j') + O(^1D)$ reaction on its electronic ground state ($^1A'$) are shown as function of collision energy in Figure 3. These probabilities are calculated for total angular momentum $J = 0$. The inset compares the TDWP results (solid lines) with the QCT results (solid circles), respectively.

Figure 3 shows that starting at low collision energy ($E_{\mathrm{col}} = 0.001$ eV ≈ 10 K) the TDWP probability for $O_2(v = 0,\ j = 0)$ rises sharply and oscillates around 0.95 up to $E_{\mathrm{col}} \sim 0.1$ eV. Afterwards, the total reaction probability decreases slowly with undulations and reaches $P \sim 0.7$ at $E_{\mathrm{col}} \sim 0.4$ eV. The non-zero probability for $E_{\mathrm{col}} \sim 10^{-3}$ eV (Figure 3) reflects

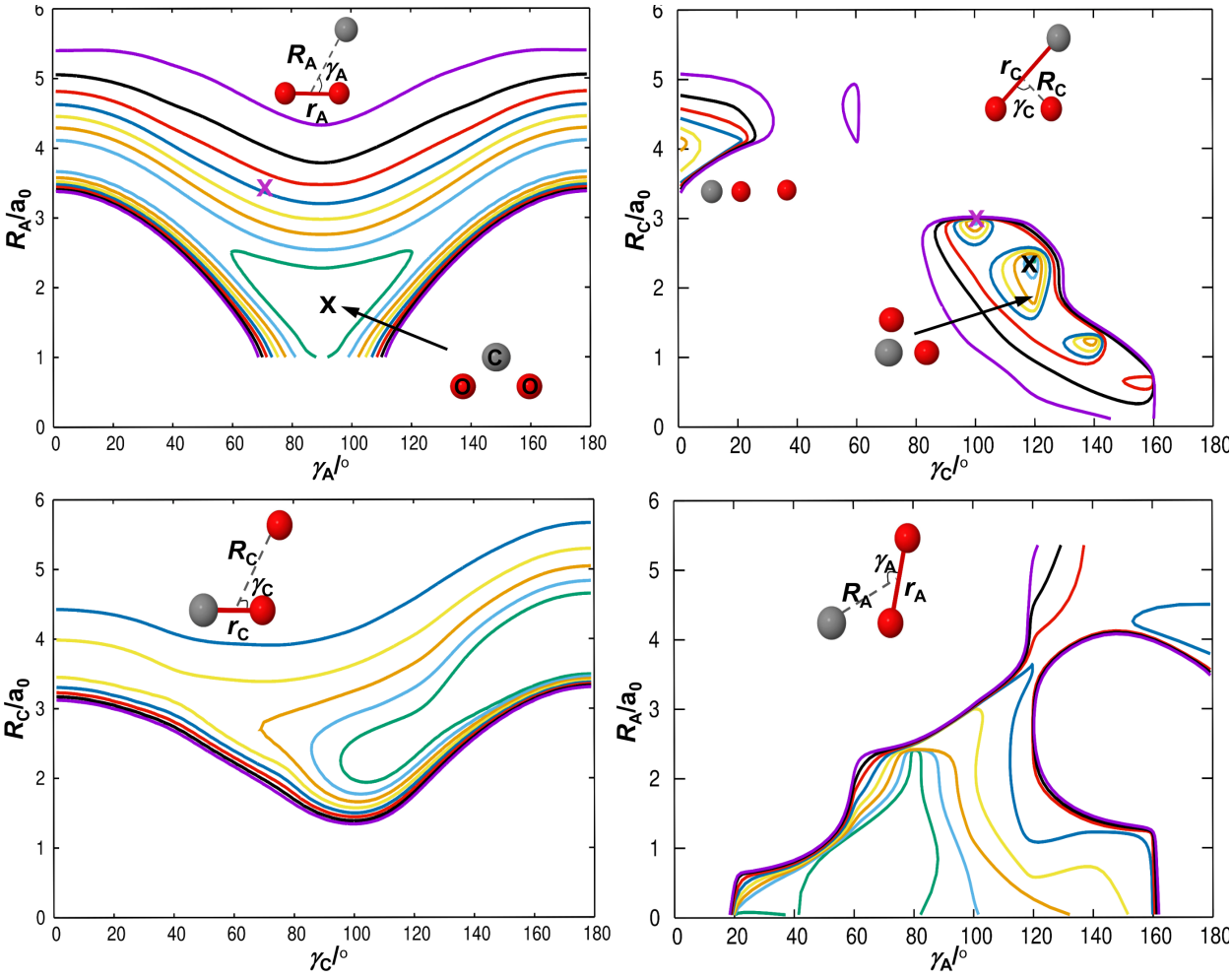

Figure 2: Two-dimensional contour diagrams of the ^{1}A′ PES for CO_2 for both Jacobi coordinate systems (reactant: R_A, γ_A) and (product: R_C, γ_C). Top: $r_{OO} =\sim 3.4$ a_0 for reactant (left) and product (right) coordinates. Bottom: $r_{CO} = 3.0$ a_0 for product (left) and reactant (right) coordinates. Contours are drawn at −2.0 eV (violet), −3.0 eV (black), −4.0 eV (red), −5.0 eV (blue), −6.0 eV (yellow), −7.0 eV (orange), −8.0 eV (cyan), −9.0 eV (green) which are with respect to the total atomization energy C(^{3}P) + O(^{3}P) + O(^{3}P). In each panel, a representative structure for CO_2 is shown in terms of the respective Jacobi coordinates. Structures for CO_2 (carbon atom grey and oxygen atoms red spheres) near the minima are schematically shown and their position on the PES is indicated with arrows. The black and purple crosses indicate equivalent geometries in the two different Jacobi coordinates.

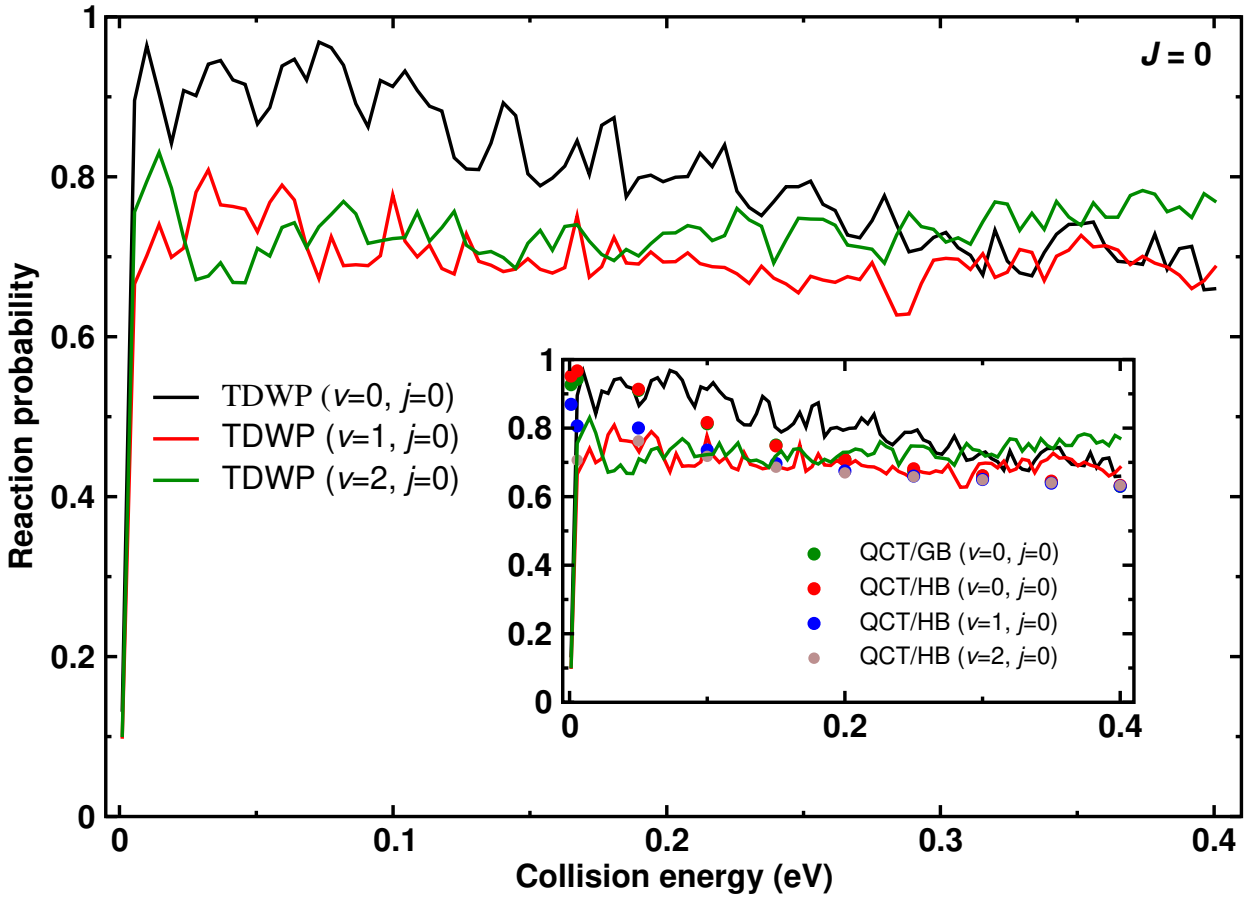

Figure 3: Initial state-selected and energy resolved total reaction probabilities of the C(^{3}P) + O$_2$($^3\Sigma_g^-$, $v = 0 - 2$, $j = 0$) $\rightarrow$ CO($^1\Sigma^+$, $\sum v'$, $\sum j'$) + O(^{1}D) reaction on its electronic ground state as a function of collision energy for $J = 0$. The TDWP and QCT probabilities are shown by solid lines and circles, respectively. The red and green circles represent the QCT results obtained by using Histogram and Gaussian binning, respectively, for O$_2$($v = 0$, $j = 0$). These probabilities at the two lowest collision energies are calculated by running 10^6 trajectories whereas 5×10^5 trajectories are used for the other energies. The QCT probabilities for O$_2$($v = 1 - 2$, $j = 0$) are shown in the inset by blue and brown solid circles.

the barrierless nature of this exoergic reaction.[21] The barrierless and exoergic features of this reaction along with the deep potential well (formation of CO_2) on the underlying PES (cf., Figure 1 of Ref. 21) and the large masses of the participating atoms make the quantum dynamical calculation computationally challenging. The undulations in the total reaction probability (see Figure 3) are indicative of formation of intermediate collision complexes inside the deep potential well.[66] However, the higher exoergicity of the reaction facilitates breakup of these complexes and thus shortens their lifetimes. Despite a deeper well on the underlying PES, lower exoergicity could change these undulations into sharp and intense resonance oscillations which was found for the S+OH, C+OH, C+H_2, and S+H_2/D_2/HD reactions.[32,43,44,67,68]

The reaction probabilities from the wavepacket simulations in Figure 3 reveal that reactant vibrational excitation decreases the reactivity at low and intermediate collision energies, whereas the reactivity is enhanced for $O_2(v = 2,\ j = 0)$ at the highest collision energies considered. Undulations for the total reaction probability are also observed for vibrationally excited reactants and analyzed further below.

Next, the reaction probabilities from the QCT simulations are considered and compared with those obtained from the TDWP approach. QCT reaction probabilities are largest for $O_2(v = 0, j = 0)$ and decay with increasing collision energy, see green (GB) and red (HB) circles in the inset of Figure 3. For $O_2(v = 1, j = 0)$ (blue circles) at low E_c the reaction probability is smaller than for $O_2(v = 0, j = 0)$ but approaches it with increasing collision energy. Interestingly, for $O_2(v = 2, j = 0)$ (brown circles) the QCT reaction probability starts low at low E_c, increases - similar to TDWP - and then also decays towards a comparable amplitude as for $v = 1$ and $v = 0$. Compared with the results from TDWP simulations the QCT simulations are in excellent overall agreement except for the lowest collision energies considered. In contrast to TDWP, the QCT results decay monotonically for higher collision energies

also for $O_2(v = 0, j = 0)$, (see inset of Figure 3). Because the wavepacket for the TDWP simulations was optimized for $O_2(v = 0)$ and not for $O_2(v = 1)$ or $O_2(v = 2)$ it is possible that the TDWP results are not fully converged at the higher collision energies considered.

3.3 Product Vibrational State Resolved Reaction Probabilities

Product vibrational level resolved reaction probabilities for $CO(v' = 0 - 17)$ and for $J = 0$ are shown in Figure 4 as a function of collision energy. The TDWP probabilities are the solid (black) lines and the QCT(HB) probabilities are the red circles. For comparison, probabilities are also determined from GB for $v' = 16 - 17$ (solid green dots) in Figure 4. Similar to the total reaction probabilities, undulations are also found in product vibrational level resolved TDWP probabilities, see Figures 3 and 4. The sharp increase of probability at the low collision energies is not found for low v'. Conversely, the TDWP probabilities for $v' = 9 - 13$ possess significant qualitative similarity with the total reaction probability.

A comparison of the state-to-state TDWP and QCT reaction probabilities in Figure 4 shows that the results are in excellent agreement with each other at all collision energies considered for $v' = 0 - 10$, which is remarkable. However, differences at low collision energies ($E_{\rm col} < 0.05$ eV) appear for $v' = 11 - 15$. Accumulation of these differences lead to the differences for the total reaction probabilities from QCT and TDWP simulations.

The two panels of Figure 4 for $CO(v' = 16, 17)$ reveal that TDWP find energy thresholds for product formation for $E_{\rm col} \sim 0.014$ and ~ 0.22 eV, respectively. This is in quite good agreement with a value of 0.19 eV for $v' = 17$ from recent QCT simulations.[21] With histogram binning for analyzing the QCT results there is no threshold for $CO(v' = 16)$ but generating $CO(v' = 17)$ requires collision energy. And analyzing the same data with GB finds thresholds for $CO(v' = 16, 17)$, see Figure 4. For the reaction with vibrational energy in the reactant

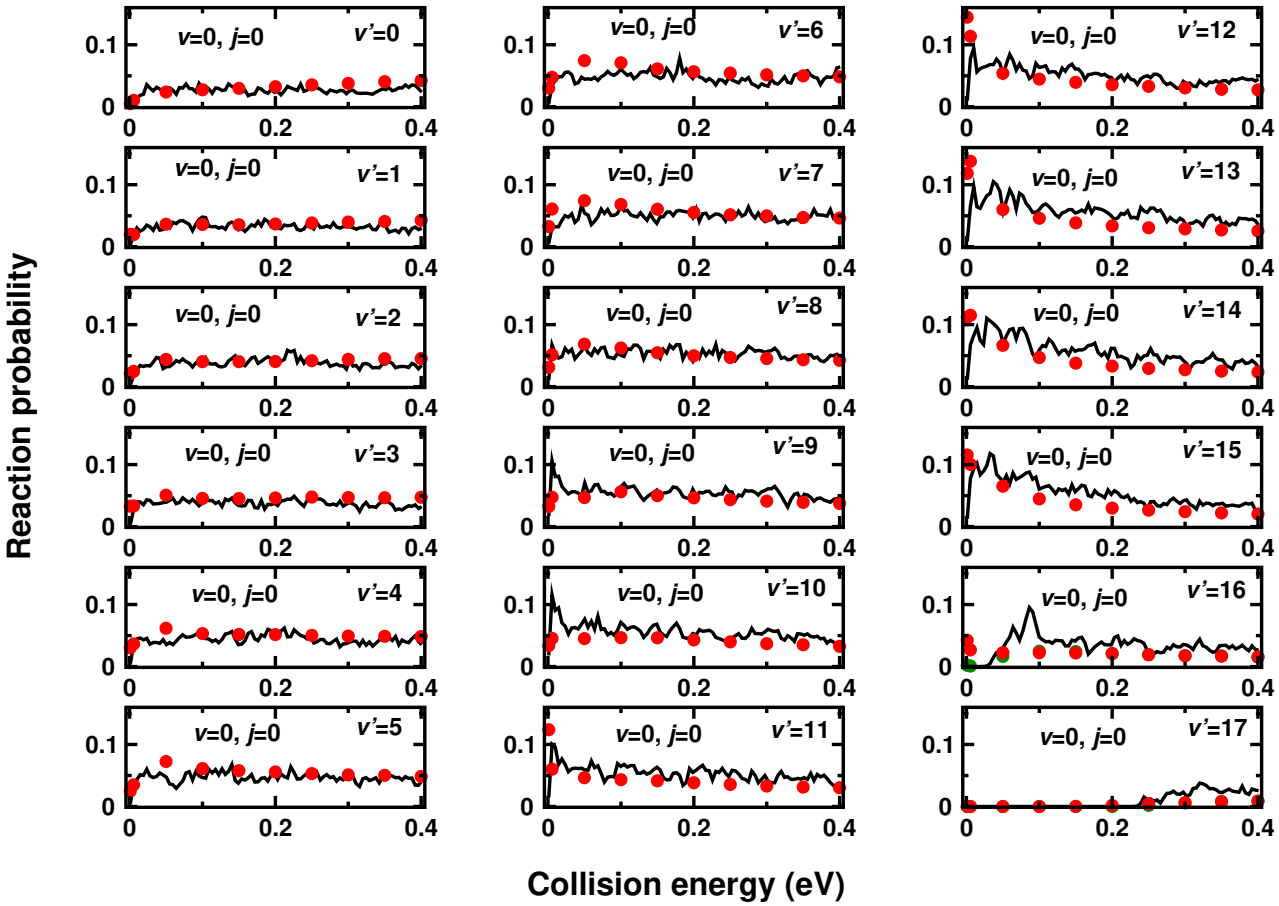

Figure 4: Product diatom vibrational level resolved state-to-state reaction probabilities for the $C(^3P) + O_2(^3\Sigma_g^-, v = 0, j = 0) \rightarrow CO(^1\Sigma^+, v', \sum j') + O(^1D)$ reaction on its electronic ground state and for $J = 0$ as function of collision energy. The probabilities calculated from the TDWP approach and QCT(HB) method are shown by solid (black) lines and solid (red) dots, respectively. Probabilities are also calculated by using QCT(GB) method for $v' = 16 - 17$ and the results are shown by solid green dots.

state (C + $O_2(v = 1, j = 0)$, see Figure **??** the product diatom vibrational level-resolved reaction probabilities from TDWP and QCT simulations compare as well as for $O_2(v = 0, j = 0)$. It can also be seen that reactant vibrational excitation has an insignificant effect on product vibrational level resolved reaction probabilities.

3.4 Product Vibrational State Distributions

The product (CO) diatom vibrational level distributions $P(v')$ at five different collision energies for the C + $O_2(v = 0-2, j = 0)$ reaction with $J = 0$ are shown in Figure 5 from TDWP (open circles) and QCT (red dots) simulations. Overall, the final state distributions from the two approaches agree favourably although $P(v')$ from QCT simulations are smoother than those from the TDWP simulations. This is particularly prevalent for low collision energies and for initial $v = 0$. With increasing vibrational excitation in the reactant $P(v')$ from the TDWP simulations also become smoother and the results from QCT overlap closely with them. Again, it may be that the results from TDWP for initial $v = 1$ and $v = 2$ are slightly affected by the fact that the initial wavepacket was optimized for $v = 0$. Compared with earlier work on the C+OH reaction the present results indicate somewhat closer agreement between the TDWP and QCT approaches, in particular with regards to pronounced minima and maxima at intermediate values of v' in $P(v')$ from the TDWP simulations.[69] It is also noteworthy to mention here that although the TDWP and QCT total reaction probabilities for $O_2(v = 2, j = 0)$ differ at higher energies (Figure 3), the vibrational distributions at $E_{\rm col} \sim 0.3$ eV and 0.4 eV agree reasonably well except for high $v' \geq 15$, see Figure 5.

It can also be seen from Figure 5 that with increasing vibrational excitation of the reactant diatom the number of product vibrational state increases. The energy supplied to reactant vibration enhances the total energy of the system and makes the opening of vibrationally excited product channels possible. This suggests that part of the reactant internal energy is

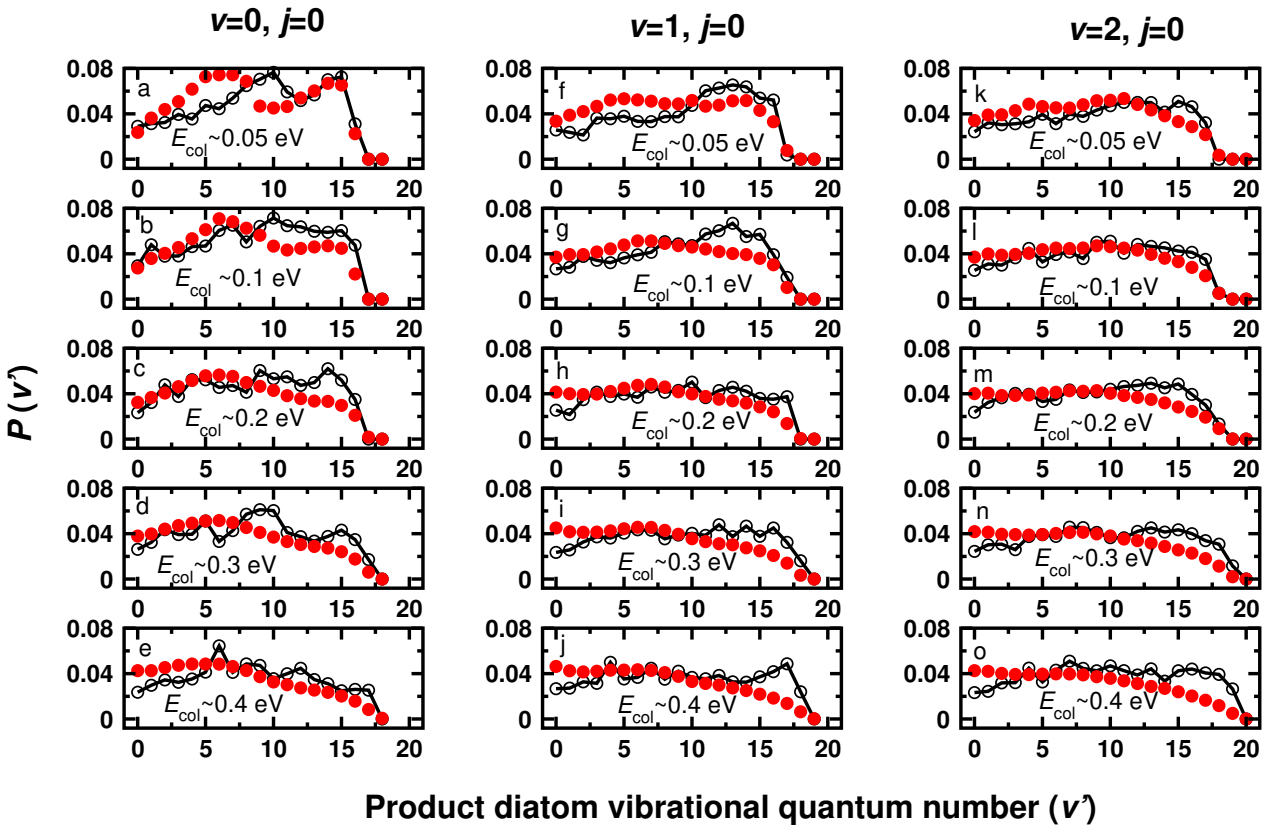

Figure 5: Product diatom vibrational level distributions at five different collision energies ($E_{\rm col}$) for the C + $O_2(v = 0 - 2, j = 0)$ reaction, by means of reaction probabilities of J =0. The results calculated by employing the TDWP and QCT approaches are shown by black lines with open circle and solid red dots, respectively. These QCT probabilities are obtained by using the HB method. The parameters of the TDWP approach were optimized for reactant $O_2(v = 0, j = 0)$ and also used for the wave packets corresponding to vibrationally excited O_2.

transferred/disposed into product vibration. However, a careful look at Figure 5 reveals that the collision energy and reactant vibrational excitation hardly have any effect on the overall pattern of the distribution and thus it becomes very difficult to find a general/regular trend for the variation of the distribution with these two types of energy.

3.5 Product rotational level distributions

The product diatom rotational level distributions $P(j')$ of the C + $O_2(v = 0 - 1,\, j = 0) \rightarrow$ CO($\sum v'$, j') +O reaction at three different collision energies ($E_{\rm col} \sim 0.05$ eV, 0.3 eV and 0.4 eV) are shown from TDWP (black bars) and QCT simulations (green lines) in Figures 6a-f. A 5-point average (red) for the TDWP distribution in each panel allows for easier comparison with the QCT results. Figure 6 shows that the agreement of the TDWP and QCT rotational distributions is excellent for moderate and high j' and also improves with increasing collision energy. Disagreement between the results from the two approaches is found for low j'. The TDWP results predict a peak at low j' which is missing in the QCT results. A possible explanation for this is the fact that low j' from QCT simulation is typically associated with separation of the two fragments from a near-collinear geometry which is unlikely to occur given the anisotropy of the PES. On the other hand, due to its spatial extent, the wavepacket samples such regions. Given the small rotational constant of the product, even small rotational energies can lead to appreciable population of low-j' states.

It can also be seen from each row of Figure 6 that reactant vibrational excitation does not change the pattern of the distributions. This is observed in both TDWP and QCT results. Thus, similar to the vibrational distributions (Figure 5), the overall pattern of the rotational distributions is also unaffected by reactant vibrational excitation. However, the peak height of the TDWP distributions at the low j' gets lowered and the distribution becomes flatter at $E_{\rm col} \sim 0.4$ eV. This is more prominent when the reactant is in its ground ro-vibrational

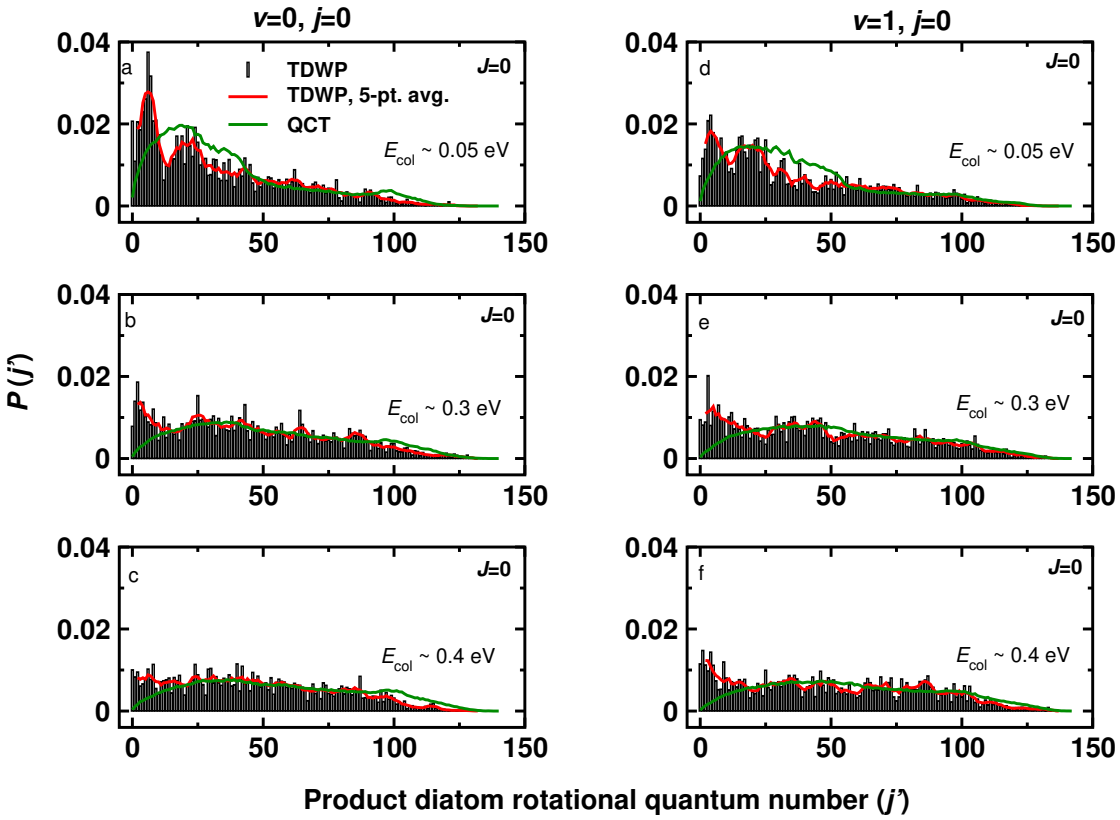

Figure 6: Product diatom rotational level distributions of the C + $O_2(v = 0 - 1,\ j = 0) \rightarrow CO(\sum v',\ j') + O$ reaction at three different collision energies ($E_{\rm col}$) as function of product diatom rotational quantum number j'. The TDWP and QCT results are shown in black bars and green line types, respectively. The red line in each panel represents a 5-point average of the TDWP distributions. The distributions for $O_2(v = 0,\ j = 0)$ and $O_2(v = 1,\ j = 0)$ are shown in panels a-c and d-f, respectively.

level. Therefore, at higher collision energies the lower and moderate j' levels of the product diatom is formed with almost equal possibility.

4 Discussion and Conclusion

The dynamics of the C + O_2 ($^3\Sigma_g^-$, $v = 0 - 2$, $j = 0$) $\rightarrow$ CO($^1\Sigma^+$, v', j') + O(^{1}D) reaction is investigated from TDWP and QCT calculations for $J = 0$ considering the ^{1}A$'$ electronic ground state. The energy resolved total reaction probabilities calculated by these two approaches are in overall excellent agreement with each other except for the lowest collision energies and for reactant $O_2(v = 2, j = 0)$ at higher energies. Enhancement of the reactivity for $O_2(v = 2, j = 0)$ at higher energies is obtained from the WP calculations whereas reactivity predicted by QCT remains insensitive to reactant vibrational excitation. This qualitative disagreement can be attributed to the possible non-convergence of the WP probabilities at the higher energies for $O_2(v = 2, j = 0)$ because the wavepacket was optimized for the $O_2(v = 0)$ ground state.

In addition to the forward C + O_2 reaction, which was the topic up to this point, the thermoneutral atom-exchange, CO_A + O_B $\rightarrow$ CO_B + O_A, and the endoergic backward CO_A + O_B $\rightarrow$ C + O_AO_B reactions also take place on the ^{1}A$'$ PES. To complete the picture, total reaction probabilities from QCT simulations for these two reactions were calculated up to 6.5 eV collision energy and the results are shown in Figure 7 as function of collision energy. It can be seen from Figure 7 that the $CO_A(v = 0, j = 0)$ + O_B $\rightarrow$ C + O_AO_B reaction has a high energy threshold whereas the atom-exchange reaction is barrierless. Comparison of probabilities shown in Figure 3 and 7 reveals that the reactivity is highest for the exoergic C + O_2 $\rightarrow$ CO + O reaction, followed by the atom-exchange reaction. The TDWP approach can also be applied here, however, the parameters shown in Table 1 need to be converged

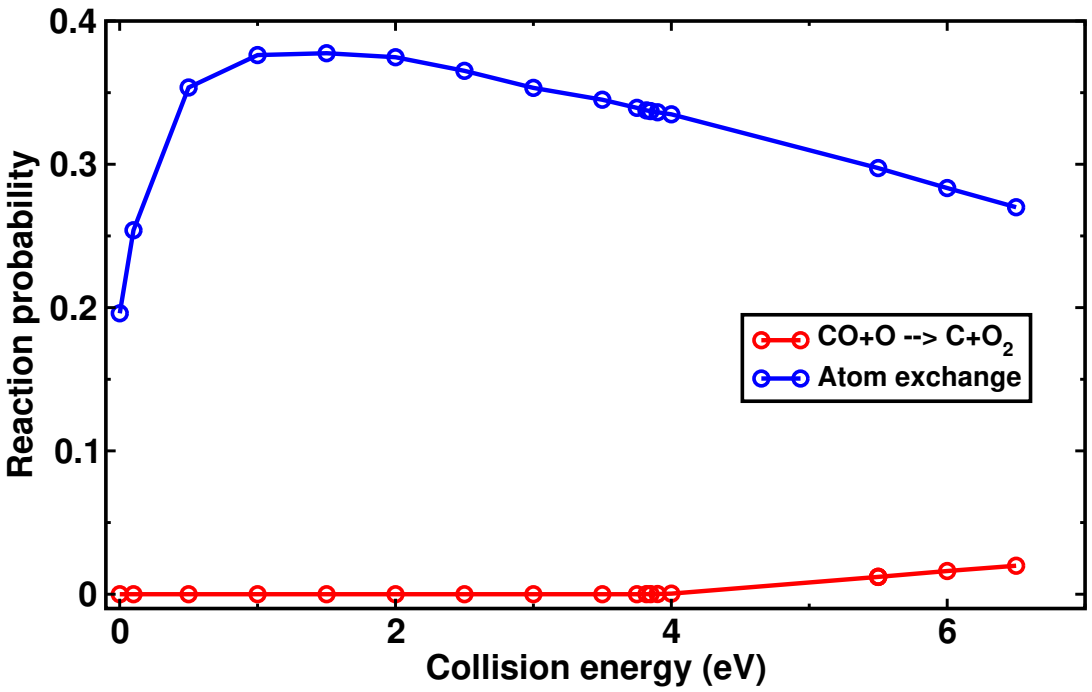

Figure 7: Energy resolved total reaction probabilities of the, $CO_A(v = 0, j = 0) + O_B \rightarrow C + O_AO_B$ and $CO_B + O_A$, reaction as function of collision energy and for J=0, calculated by employing the QCT approach.

separately for the atom-exchange and endoergic backward reactions which is outside the scope of the present work. Given the good agreement between TDWP and QCT simulations it is, however, expected that the results from Figure 7 are representative.

The thermoneutral atom-exchange reaction ($CO_A + O_B \rightarrow CO_B + O_A$) has already been considered in the context of stabilizing CO_2 on amorphous solid water (ASW) to better understand molecule formation at astrophysical conditions.[70,71] For this process it was found that for bulk temperatures of $\sim$ 50 K formation and stabilization of CO_2 is very likely (60 % of the trajectories stabilize). Together with the present results this suggests that quantum effects will only marginally affect this conclusion. This is also consistent with results from QCT and TDWP simulations for $O(^3P)+O(^3P)$ recombination for which quantum mechanical effects were also found to be far less important than effects of ASW surface roughness on the diffusivity and recombination dynamics.[72,73]

The undulations in the total reaction probabilities from TDWP simulations (Figures 3, 4 and **??**) are attributed to formation and transient stabilization of the CO_2 intermediate inside the potential well. These are largely unaffected by reactant vibrational excitation, and merit some further discussion. Based on earlier work[66] these undulations can be associated with formation of a transiently stabilized CO_2 intermediate. Large undulations with some resonances were found in the QM total reaction probabilities of the exoergic and barrierless N + OH $\rightarrow$ NO + H reaction proceeding through deep HON well on the underlying PES.[66] Furthermore, dense resonance structures are found between 0.41 and 0.43 eV collision energies.[66] The authors have associated these resonances to the formation of long-lived intermediate complex inside the HON potential well.[66] The exoergicities of the N + OH and present C + O_2 reactions are 1.99 eV and $\sim$ 3.8 eV. Therefore, large undulations are found in the reaction probabilities of the present C + O_2 reaction due to the formation of transiently stabilized CO_2 intermediate inside the potential well on the underlying PES.

The black-solid curve in Figure 3 shows that there are 19 prominent peaks across the entire range of collision energies considered. Peak separations range from $\sim$ 0.009 eV to $\sim$ 0.036 eV with an average of $\sim$ 0.021 eV. Using the energy/time uncertainty relationship $\Delta E \times \Delta t = \hbar$, corresponding lifetimes range from $\sim$ 0.018 ps to $\sim$ 0.073 ps with an average of $\sim$ 0.038 ps.

The three internuclear separations from representative QCT simulations for $E_{\rm col} = 0.05$ eV and $E_{\rm col} = 0.40$ eV are shown in Figure 8 and the corresponding collision time distributions $P(\tau_{\rm c})$ are reported in Figure 9. Here, $\tau_{\rm c}$ is defined as the time for which the sum of the three internuclear distances is smaller than 14 a_0 or 12 a_0, respectively. The distribution $P(\tau_{\rm c})$ was determined from 22000 reactive trajectories at each of the collision energies. The time series in Figures 8a and d represent trajectories with short collision time $\tau_{\rm c} \sim 0.03$ ps and $\sim$ 0.04 ps, respectively, whereas Figures 8b and e show trajectories with longer $\tau_{\rm c}$

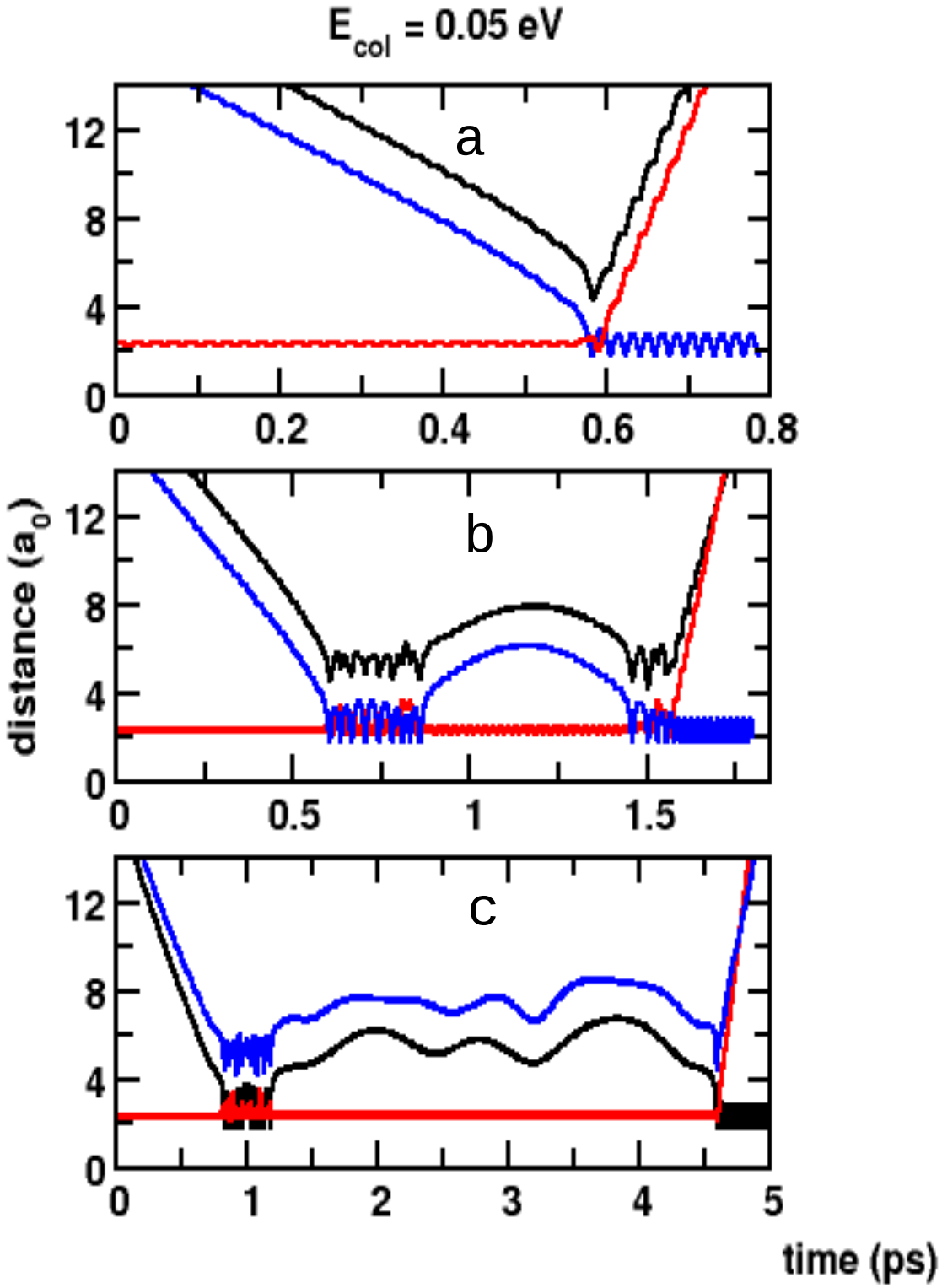

Figure 8: Time evolution of the inter nuclear distances of the three diatoms, O_2 (red), CO_A (blue) and CO_B (black) as function of time for $E_{col} = 0.05$ eV (left column) and $E_{col} = 0.40$

(∼ 1.0 ps and ∼ 1.02 ps, respectively). The results of panels b and e clearly indicate the formation of triatomic intermediate complexes whereas the findings of panels c and f suggest the formation of weakly bound triatomic complexes with short contact times, reminiscent of roaming.

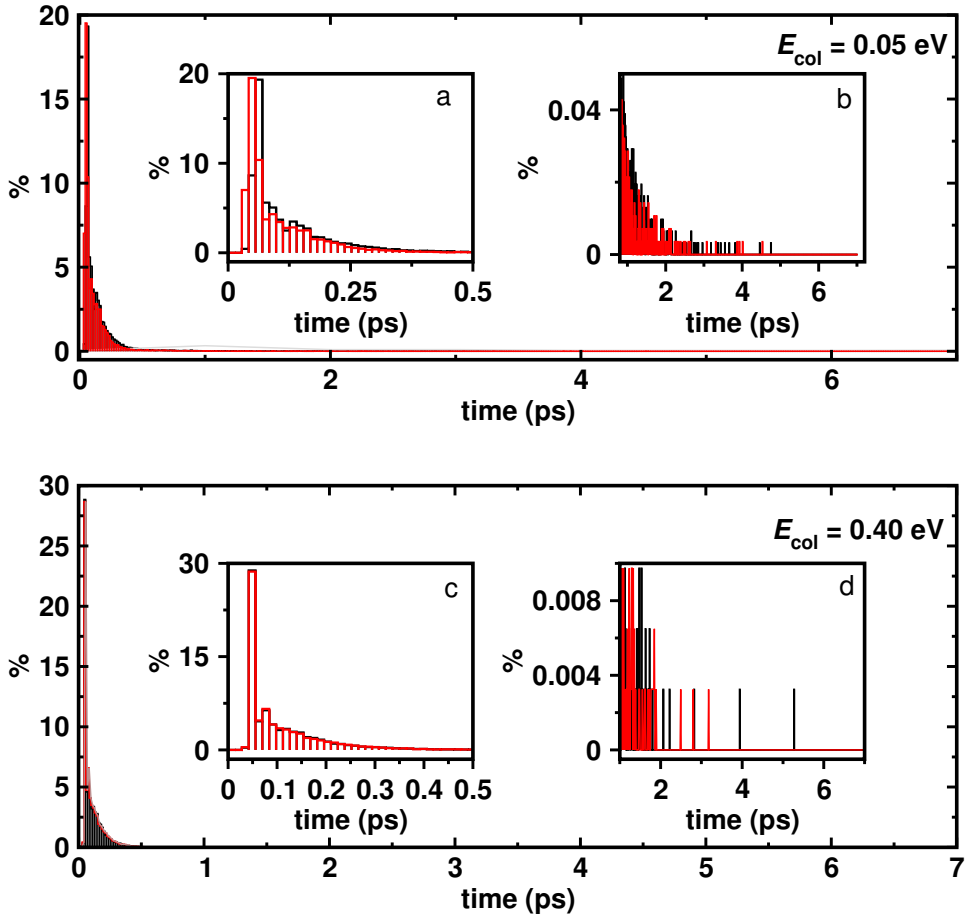

Figure 9: Distributions of collision time (or lifetime) of the intermediate collision complex as function of time analyzed with a cutoff of 14 a_0 (black) and 12 a_0 (red) for the sum of distances as the criterion for formation of the complex. The distributions at 0.05 eV and 0.40 eV collision energies are shown in the top and bottom panels, respectively, together with detailed views for short and long collision times in the insets. The maxima for the two distributions with a distance cutoff at 14 a_0 are at ∼ 0.07 ps and ∼ 0.056 ps and the longest collision times encountered are ∼ 4.8 ps and ∼ 5.3 ps for the two cases considered. These values change to ∼ 0.056 ps and ∼ 0.056 ps and ∼ 4.5 ps and ∼ 3.2 ps for the maxima and longest collision time, respectively, if a cutoff of 12 a_0 is used.

The collision time distributions from QCT simulations are strongly peaked with their max-

ima at $\tau_c \sim 0.07$ ps and ~ 0.056 ps for $E_{col} = 0.05$ eV and 0.40 eV, respectively, see inset of Figure 9. The probability for finding such short collision times is 20 % and 30 %, respectively, for the two collision energies considered. If a shorter distance cutoff of 12 a_0 is used the maxima of $P(\tau_c)$ are at $\tau_c = 0.056$ ps whereas the longest lifetimes are 4.5 ps and 3.2 ps for the two collision energies. Hence, the analysis of the lifetimes is only moderately affected by the choice of the cutoff value for the sum of the three interatomic distances.

Collision times of the order of 0.06 ps are in quite good qualitative agreement with the analysis of the recurrences in the reaction probabilities from TDWP simulations which yielded lifetimes of around $\sim$ 0.04 ps, see above. On the other hand, the QCT simulations also find a long tail in the collision time distributions extending out to $\sim$ 4.8 ps and $\sim$ 5.3 ps for the longest collision times for the two simulation conditions considered. Overall, it is found that the implied time scales of the undulations in the TDWP reaction probabilities, which have previously been linked to formation of a collisionally stabilized intermediate,[66] are consistent with the collision times from the QCT simulations, and that they constitute an inherent characteristic of the reaction considered.

The agreement between the TDWP and QCT product vibrational level resolved probabilities for $O_2(v = 0 - 1,\ j = 0)$ is remarkably good except for low E_{col} and only for specific values of v'. Reactant vibrational excitation does not change the pattern of these state-to-state probabilities significantly. For the product rotational level distributions at different collision energies, the agreement between TDWP and QCT results is excellent for moderate and higher $j' \gtrsim 15$ values and improves with increasing collision energy. The peak in $P(j')$ from TDWP simulations at low j' is not obtained from the QCT calculations and reactant vibrational excitation has little impact on the overall behaviour of the final state distribution.

The present results can also be compared with results from pulsed, crossed, supersonic molec-

ular beams, at relative translational energies between 4.4 and 90 meV.[74] Such experiments found that collision energy $E_c > 0.04$ eV is required to open the product CO($v' = 17$) channel. For CO($v' = 17$), the present QCT investigation shows a threshold of ~ 0.15 eV from analysis based on histogram and ~ 0.25 eV from Gaussian binning, respectively. An earlier QCT investigation[21] on a finer grid for E_c showed that for ($v = 0$, $j < 10$) the threshold is 0.18 eV which changes to 0.25 eV if the same data is analyzed for ($v = 0$, $j = 0$). This is also consistent with ~ 0.22 eV from the TDWP simulations. Including higher rotational states for the reactant progressively shift the threshold to 0.04 eV when all reactant $j-$states are included which agrees well with the experiments.[21,74]

In summary, this work provides a stringent comparison for total and product diatom vibrational state resolved reaction probabilities and product state vibrational and rotational distributions from TDWP and QCT simulations for the C+O_2 $\rightarrow$ O+CO reaction on its ground electronic state. Overall, the agreement of a quasi-classical description with results from wavepacket simulations is encouraging except for the lowest collision energies or lowest product rotational states. Expected quantum effects such as undulations in the total reaction probability $P(E_c)$ can be rationalized in a qualitative fashion from analysis of the QCT trajectories. Given the ease with which QCT simulations can be carried out the present work suggests that they are a meaningful approach for understanding the dynamics of atom plus diatom reactions and for larger systems as well.

Acknowledgments

Support by the Swiss National Science Foundation through grants 200021-117810, the NCCR MUST (to MM), and the University of Basel is acknowledged. Part of this work was supported by the United State Department of the Air Force, which is gratefully acknowledged

(to MM). This project has received funding from the European Union Horizon 2020 funding scheme under MCSA Grant No 801459, FP-RESOMUS.

References

(1) Sharma, M.; Swantek, A. B.; Flaherty, W.; Austin, J. M.; Doraiswamy, S.; Candler, G. V. Experimental and Numerical Investigation of Hypervelocity Carbon Dioxide Flow over Blunt Bodies. *J. Thermophys. Heat Transf.* **2010**, *24*, 673–683.

(2) Husain, D.; Young, A. N. Kinetic investigation of ground state carbon atoms, C(2^3P). *J. Chem. Soc., Faraday Trans. 2* **1975**, *71*, 525–531.

(3) Bergeat, A.; Calvo, T.; Dorthe, G.; Loison, J. Fast-flow study of the C+NO and C+O_2 reactions. *Chem. Phys. Lett.* **1999**, *308*, 7–12.

(4) Geppert, W. D.; Reignier, D.; Stoecklin, T.; Naulin, C.; Costes, M.; Chastaing, D.; Le Picard, S. D.; Sims, I. R.; Smith, I. W. M. Comparison of the cross-sections and thermal rate constants for the reactions of C(^{3}P) atoms with O_2 and NO. *Phys. Chem. Chem. Phys.* **2000**, *2*, 2873–2881.

(5) Becker, K. H.; Brockmann, K. J.; Weisen, P. Spectroscopic identification of C(^{3}P) atoms in halogenomethane + H flame systems and measurements of C(^{3}P) reaction rate constants by two-photon laser-induced fluorescence. *J. Chem. Soc. Faraday Trans. 2* **1988**, *84*, 455–461.

(6) Dorthe, G.; Caubet, P.; Vias, T.; Barrere, B.; Marchais, J. Fast flow studies of atomic carbon kinetics at room temperature. *J. Phys. Chem.* **1991**, *95*, 5109–5116.

(7) Chastaing, D.; L. James, P.; R. Sims, I.; W. M. Smith, I. Neutral–neutral reactions at the temperatures of interstellar clouds: Rate coefficients for reactions of atomic carbon,

C(^{3}P), with O_2, C_2H_2, C_2H_4 and C_3H_6 down to 15 K. *Phys. Chem. Chem. Phys.* **1999**, *1*, 2247–2256.

(8) Chastaing, D.; Le Picard, S. D.; Sims, I. R. Direct kinetic measurements on reactions of atomic carbon, C(^{3}P), with O_2 and NO at temperatures down to 15 K. *J. Chem. Phys.* **2000**, *112*, 8466–8469.

(9) Dean, A. J.; Davidson, D. F.; Hanson, R. K. A shock tube study of reactions of C atoms with H_2 and O_2 using excimer photolysis of C_3O_2 and C atom atomic resonance absorption spectroscopy. *J. Phys. Chem.* **1991**, *95*, 183–191.

(10) Ogryzlo, E.; Reilly, J.; Thrush, B. Vibrational excitation of CO from the reaction C+ O_2. *Chem. Phys. Lett.* **1973**, *23*, 37–39.

(11) Dubrin, J.; MacKay, C.; Pandow, M.; Wolfgang, R. Reactions of atomic carbon with π-bonded inorganic molecules. *J. Inorg. Nuc. Chem.* **1964**, *26*, 2113–2122.

(12) Xantheas, S. S.; Ruedenberg, K. Potential energy surfaces of carbon dioxide. *Int. J. Quantum Chem.* **1994**, *49*, 409–427.

(13) Jasper, A. W.; Dawes, R. Non-Born–Oppenheimer molecular dynamics of the spin-forbidden reaction O(^{3}P) + CO($X^1\Sigma^+$) $\rightarrow$ $CO_2(X^1\Sigma_g^+)$. *J. Chem. Phys.* **2013**, *139*, 154313.

(14) Troe, J. Thermal dissociation and recombination of polyatomic molecules. *Fifth Symp. (Int.) Combust.* **1975**, *15*, 667–679.

(15) Braunstein, M.; Duff, J. W. Electronic structure and dynamics of O(^{3}P) + CO($^1\Sigma^+$) collisions. *J. Chem. Phys.* **2000**, *112*, 2736–2745.

(16) Kozlov, P.; Makarov, V.; Pavlov, V.; Shatalov, O. Experimental investigation of CO vibrational deactivation in a supersonic cooling gas flow. *Shock Waves* **2000**, *10*, 191–195.

(17) Center, R. E. Vibrational relaxation of CO by O atoms. *J. Chem. Phys.* **1973**, *58*, 5230–5236.

(18) Kelley, J. D.; Thommarson, R. L. Vibrational deactivation and atom exchange in $O(^3P)$ + $CO(X^1\Sigma^+)$ collisions. *J. Chem. Phys.* **1977**, *66*, 1953–1959.

(19) Davidson, J. A.; Schiff, H. I.; Brown, T. J.; Howard, C. J. Temperature dependence of the deactivation of $O(^1D)$ by CO from 113-333 K. *J. Chem. Phys.* **1978**, *69*, 1216–1217.

(20) Tully, J. C. Reactions of $O(^1D)$ with atmospheric molecules. *J. Chem. Phys.* **1975**, *62*, 1893–1898.

(21) San Vicente Veliz, J. C.; Koner, D.; Schwilk, M.; Bemish, R. J.; Meuwly, M. The $C(^3P)$ + $O_2(^3\Sigma_g^-) \longleftrightarrow CO_2 \longleftrightarrow CO(^1\Sigma^+)$ + $O(^1D)/O(^3P)$ reaction: thermal and vibrational relaxation rates from 15 K to 20000 K. *Phys. Chem. Chem. Phys.* **2021**, *23*, 11251–11263.

(22) Winter, N. W.; Bender, C. F.; Goddard III, W. A. Theoretical assignments of the low-lying electronic states of carbon dioxide. *Chem. Phys. Lett.* **1973**, *20*, 489–492.

(23) Grebenshchikov, S. Y.; Borrelli, R. Crossing Electronic States in the Franck-Condon Zone of Carbon Dioxide: A Five-Fold Closed Seam of Conical and Glancing Intersections. *J. Phys. Chem. Lett.* **2012**, *3*, 3223–3227.

(24) Grebenshchikov, S. Y. Photodissociation of carbon dioxide in singlet valence electronic states. II. Five state absorption spectrum and vibronic assignment. *J. Chem. Phys.* **2013**, *138*, 224107.

(25) Grebenshchikov, S. Y. Photodissociation of carbon dioxide in singlet valence electronic states. I. Six multiply intersecting ab initio potential energy surfaces. *J. Chem. Phys.* **2013**, *138*, 224106.

(26) Schmidt, J. A.; Johnson, M. S.; Schinke, R. Carbon dioxide photolysis from 150 to 210 nm: Singlet and triplet channel dynamics, UV-spectrum, and isotope effects. *Proc. Natl. Acad. Sci.* **2013**, *110*, 17691–17696.

(27) Zhou, B.; Zhu, C.; Wen, Z.; Jiang, Z.; Yu, J.; Lee, Y.-P.; Lin, S. H. Topology of conical/surface intersections among five low-lying electronic states of CO_2: Multireference configuration interaction calculations. *J. Chem. Phys.* **2013**, *139*.

(28) Kinnersly, S.; Murrell, J. A classical dynamical study of the reaction between C(^{3}P) and $O_2(^3\Sigma_g^-)$. *Mol. Phys.* **1977**, *33*, 1479–1494.

(29) Brunsvold, A. L.; Upadhyaya, H. P.; Zhang, J.; Cooper, R.; Minton, T. K.; Braunstein, M.; Duff, J. W. Dynamics of Hyperthermal Collisions of O(^{3}P) with CO. *J. Phys. Chem. A* **2008**, *112*, 2192–2205.

(30) Koner, D.; Bemish, R. J.; Meuwly, M. Dynamics on multiple potential energy surfaces: quantitative studies of elementary processes relevant to hypersonics. *J. Phys. Chem. A* **2020**, *124*, 6255–6269.

(31) Zanchet, A.; Bussery-Honvault, B.; Jorfi, M.; Honvault, P. Study of the C(^{3}P)+ OH($X^2\Pi$)$\rightarrow$ CO($a^3\Pi$)+ H(^{2}S) reaction: fully global ab initio potential energy surfaces of the 1^2A" and 1^4A" excited states and non adiabatic couplings. *Phys. Chem. Chem. Phys.* **2009**, *11*, 6182–6191.

(32) Goswami, S.; Rao, T. R.; Mahapatra, S.; Bussery-Honvault, B.; Honvault, P. Time-dependent quantum wave packet dynamics of S + OH reaction on its electronic ground state. *J. Phys. Chem. A* **2014**, *118*, 5915–5926.

(33) Jorfi, M.; Honvault, P.; Halvick, P. Quasi-classical determination of integral cross-sections and rate constants for the N+ OH $\rightarrow$ NO+ H reaction. *Chem. Phys. Lett.* **2009**, *471*, 65–70.

(34) Jorfi, M.; Honvault, P.; Halvick, P. Quasiclassical trajectory calculations of differential cross sections and product energy distributions for the N+ OH → NO+ H reaction. *J. Chem. Phys.* **2009**, *131*, 094302.

(35) Jorfi, M.; Honvault, P.; Bargueño, P.; González-Lezana, T.; Larrégaray, P.; Bonnet, L.; Halvick, P. On the statistical behavior of the O+ OH → H+ O_2 reaction: A comparison between quasiclassical trajectory, quantum scattering, and statistical calculations. *J. Chem. Phys.* **2009**, *130*, 184301.

(36) Jorfi, M.; Honvault, P. Quantum dynamics at the state-to-state level of the C+OH reaction on the first excited potential energy surface. *J. Phys. Chem. A* **2010**, *114*, 4742–4747.

(37) Jorfi, M.; Honvault, P. State-to-state quantum dynamics calculations of the C+OH reaction on the second excited potential energy surface. *J. Phys. Chem. A* **2011**, *115*, 8791–8796.

(38) Rao, T. R.; Goswami, S.; Mahapatra, S.; Bussery-Honvault, B.; Honvault, P. Time-dependent quantum wave packet dynamics of the C + OH reaction on the excited electronic state. *J. Chem. Phys.* **2013**, *138*, 094318.

(39) Jorfi, M.; Honvault, P. Quasi-classical trajectory study of the S+OH → SO+H reaction: from reaction probability to thermal rate constant. *Phys. Chem. Chem. Phys.* **2011**, *13*, 8414–8421.

(40) Panda, A. N.; Herráez-Aguilar, D.; Jambrina, P. G.; Aldegunde, J.; Althorpe, S. C.; Aoiz, F. J. A state-to-state dynamical study of the Br + H_2 reaction: comparison of quantum and classical trajectory results. *Phys. Chem. Chem. Phys.* **2012**, *14*, 13067–13075.

(41) Bargueño, P.; Jambrina, P.; Alvariño, J. M.; Menéndez, M.; Verdasco, E.; Hankel, M.; Smith, S.; Aoiz, F. J.; González-Lezana, T. Energy dependent dynamics of the O(^{1}D)

+ HCl reaction: A quantum, quasiclassical and statistical study. *Phys. Chem. Chem. Phys.* **2011**, *13*, 8502–8514.

(42) Hankel, M.; Yue, X.-F. Quantum dynamics study of the N(^{2}D) + H_2 reaction and the effects of the potential energy surface on the propagation time. *Comput. Theor. Chem.* **2012**, *990*, 23–29.

(43) Goswami, S.; Bussery-Honvault, B.; Honvault, P.; Mahapatra, S. Effect of internal excitations of reagent diatom on initial state-selected dynamics of C + OH reaction on its second excited (1^4A$''$) electronic state. *Mol. Phys.* **2017**, *115*, 2658–2672.

(44) Goswami, S.; Sahoo, J.; Rao, T. R.; Bussery-Honvault, B.; Honvault, P.; Mahapatra, S. A theoretical study on the C + OH reaction dynamics and product energy disposal with vibrationally excited reagent. *Eur. Phys. J. D* **2018**, *72*, 1–19.

(45) Polanyi, J. Some concepts in reaction dynamics. *Acc. Chem. Res.* **1972**, *5*, 161.

(46) Jiang, B.; Guo, H. Relative efficacy of vibrational vs. translational excitation in promoting atom-diatom reactivity: Rigorous examination of Polanyi's rules and proposition of sudden vector projection (SVP) model. *J. Chem. Phys.* **2013**, *138*, 234104.

(47) Polanyi, J. C. Some concepts in reaction dynamics. *Science* **1987**, *236*, 680–690.

(48) Bulut, N.; Roncero, O.; Jorfi, M.; Honvault, P. Accurate time dependent wave packet calculations for the N+OH reaction. *J. Chem. Phys.* **2011**, *135*, 104307.

(49) Lin, S. Y.; Guo, H.; Honvault, P.; Xu, C.; Xie, D. Accurate quantum mechanical calculations of differential and integral cross sections and rate constant for the O+ OH reaction using an ab initio potential energy surface. *J. Chem. Phys.* **2008**, *128*, 014303.

(50) Hankel, M.; Smith, S. C.; Gray, S. K.; Balint-Kurti, G. G. DIFFREALWAVE: A parallel real wavepacket code for the quantum mechanical calculation of reactive state-to-

state differential cross sections in atom plus diatom collisions. *Comput. Phys. Commun.* **2008**, *179*, 569–578.

(51) Gray, S. K.; Balint-Kurti, G. G. Quantum dynamics with real wave packets, including application to three-dimensional ($J = 0$) D+H_2 →HD+H reactive scattering. *J. Chem. Phys.* **1998**, *108*, 950–962.

(52) Hankel, M.; Smith, S. C.; Allan, R. J.; Gray, S. K.; Balint-Kurti, G. G. State-to-state reactive differential cross sections for the H + H_2 → H_2 + H reaction on five different potential energy surfaces employing a new quantum wavepacket computer code: DIFFREALWAVE. *J. Chem. Phys.* **2006**, *125*, 164303.

(53) Goswami, S.; Sahoo, J.; Paul, S. K.; Rao, T. R.; Mahapatra, S. Effect of Reagent Vibration and Rotation on the State-to-State Dynamics of the Hydrogen Exchange Reaction, H + H_2 → H_2+ H. *J. Phys. Chem. A* **2020**, *124*, 9343–9359.

(54) Hankel, M.; Balint-Kurti, G. G.; Gray, S. K. Sinc wave packets: New form of wave packet for time-dependent quantum mechanical reactive scattering calculations. *Int. J Quantum Chem.* **2003**, *92*, 205–211.

(55) Offer, A. R.; Balint-Kurti, G. G. Time-dependent quantum mechanical study of the photodissociation of HOCl and DOCl. *J. Chem. Phys.* **1994**, *101*, 10416–10428.

(56) Kosloff, D.; Kosloff, R. A Fourier method solution for the time dependent Schrödinger equation as a tool in molecular dynamics. *J. Comput. Phys.* **1983**, *52*, 35–53.

(57) Light, J.; Hamilton, I.; Lill, J. Generalized discrete variable approximation in quantum mechanics. *J. Chem. Phys.* **1985**, *82*, 1400–1409.

(58) Lill, J.; Parker, G.; Light, J. Discrete variable representations and sudden models in quantum scattering theory. *Chem. Phys. Lett.* **1982**, *89*, 483–489.

(59) Hamilton, I.; Light, J. On distributed Gaussian bases for simple model multidimensional vibrational problems. *J. Chem. Phys.* **1986**, *84*, 306–317.

(60) Henriksen, N. E.; Hansen, F. Y. *Theories of Molecular Reaction Dynamics*; Oxford, 2011.

(61) Koner, D.; Barrios, L.; González-Lezana, T.; Panda, A. N. State-to-State Dynamics of the Ne + $HeH^+(v = 0, j = 0) \rightarrow NeH^+(v', j')$ + He Reaction. *J. Phys. Chem. A* **2016**, *120*, 4731–4741.

(62) Koner, D.; Bemish, R. J.; Meuwly, M. The $C(^3P)$ + $NO(X^2\Pi) \rightarrow O(^3P)$ + $CN(X^2\Sigma^+)$, $N(^2D)/N(^4S)$ + $CO(X^1\Sigma^+)$ reaction: Rates, branching ratios, and final states from 15 K to 20 000 K. *J. Chem. Phys.* **2018**, *149*, 094305.

(63) Truhlar, D. G.; Muckerman, J. T. In *Atom - Molecule Collision Theory*; Bernstein, R. B., Ed.; Springer US, 1979; pp 505–566.

(64) Bonnet, L.; Rayez, J.-C. Quasiclassical Trajectory Method for Molecular Scattering Processes: Necessity of a Weighted Binning Approach. *Chem. Phys. Lett.* **1997**, *277*, 183–190.

(65) Bonnet, L.; Rayez, J.-C. Gaussian Weighting in the Quasiclassical Trajectory Method. *Chem. Phys. Lett.* **2004**, *397*, 106–109.

(66) Jorfi, M.; Honvault, P. State-to-state quantum dynamical study of the N + OH $\rightarrow$ NO + H reaction. *J. Phys. Chem. A* **2009**, *113*, 2316–2322.

(67) Bañares, L.; Aoiz, F.; Honvault, P.; Bussery-Honvault, B.; Launay, J.-M. Quantum mechanical and quasi-classical trajectory study of the $C(^1D)$ + H_2 reaction dynamics. *J. Chem. Phys.* **2003**, *118*, 565–568.

(68) Banares, L.; Castillo, J.; Honvault, P.; Launay, J.-M. Quantum mechanical and quasiclassical trajectory reaction probabilities and cross sections for the S(^{1}D) + H_2, D_2, HD insertion reactions. *Phys. Chem. Chem. Phys.* **2005**, *7*, 627–634.

(69) Bulut, N.; Zanchet, A.; Honvault, P.; Bussery-Honvault, B.; Bañares, L. Time-dependent wave packet and quasiclassical trajectory study of the C(^{3}P)+OH($X^2\Pi$)→ CO($X^1\Sigma^+$)+H(^{2}S) reaction at the state-to-state level. *J. Chem. Phys.* **2009**, *130*, 194303.

(70) Upadhyay, M.; Pezzella, M.; Meuwly, M. Genesis of Polyatomic Molecules in Dark Clouds: CO2 Formation on Cold Amorphous Solid Water. *J. Phys. Chem. Lett.* **2021**, *12*, 6781–6787.

(71) Upadhyay, M.; Meuwly, M. Energy Redistribution Following CO2 Formation on Cold Amorphous Solid Water. *Frontiers in chemistry* **2021**, *9*.

(72) Pezzella, M.; Unke, O. T.; Meuwly, M. Molecular Oxygen Formation in Interstellar Ices Does Not Require Tunneling. *J. Phys. Chem. Lett.* **2018**, *9*, 1822–1826.

(73) Pezzella, M.; Koner, D.; Meuwly, M. Formation and Stabilization of Ground and Excited-State Singlet O_2 upon Recombination of ^{3}P Oxygen on Amorphous Solid Water. *J. Phys. Chem. Lett.* **2020**, *11*, 2171–2176.

(74) Costes, M.; Naulin, C. State-to-state cross sections for the C(^3P_J)+ $O_2(X^3\Sigma_g^-)$ → CO($X^1\Sigma^+$)+ O($^1D_2$) reaction at kinetic energies between 4.4 and 90 meV. *Comptes Rendus de l'Académie des Sciences-Series IIC-Chemistry* **1998**, *1*, 771–775.